

Analog quantum simulation of the Rabi model in the ultra-strong coupling regime

Jochen Braumüller,^{1,*} Michael Marthaler,² Andre Schneider,¹ Alexander Stehli,¹ Hannes Rotzinger,¹ Martin Weides,^{1,3} and Alexey V. Ustinov^{1,4}

¹*Physikalisches Institut, Karlsruhe Institute of Technology, 76131 Karlsruhe, Germany*

²*Institut für Theoretische Festkörperphysik, Karlsruhe Institute of Technology, 76131 Karlsruhe, Germany*

³*Physikalisches Institut, Johannes Gutenberg University Mainz, 55128 Mainz, Germany*

⁴*Russian Quantum Center, National University of Science and Technology MISIS, Moscow 119049, Russia*

(Dated: November 28, 2016)

The quantum Rabi model describes the fundamental mechanism of light-matter interaction. It consists of a two-level atom or qubit coupled to a quantized harmonic mode via a transversal interaction. In the weak coupling regime, a rotating wave approximation can be applied and the quantum Rabi Hamiltonian reduces to the well-known Jaynes-Cummings Hamiltonian. In the ultra-strong coupling regime, where the effective coupling strength g is comparable to the energy ω of the bosonic mode, the counter rotating terms can no longer be neglected, revealing remarkable features in the system dynamics. Here, we demonstrate an analog quantum simulation of the quantum Rabi model in the ultra-strong coupling regime of variable strength. The quantum hardware of the simulator is a superconducting circuit embedded in a cQED setup. The simulation scheme is based on the application of two transversal microwave drive tones used to engineer the desired effective Hamiltonian. We observe a fast quantum state collapse followed by periodically recurring quantum revivals of the initial qubit state, which is the most distinct signature of the synthesized model. We achieve a relative coupling ratio of $g/\omega \sim 0.7$, approaching the deep strong coupling regime.

Introduction.— Finding solutions to many quantum problems is a very challenging task [1]. The reason is the exponentially large number of degrees of freedom in a quantum system, requiring computational power and memory that easily exceed the capabilities of present classical computers. A yet to be demonstrated universal digital quantum computer of sufficient size would be capable of efficiently solving most quantum problems [1, 2]. A more feasible approach to achieve a computational speedup in the near future is quantum simulation [1–3]. In the framework of analog quantum simulation, a tailored and well-controllable artificial quantum system is mapped onto a quantum problem of interest in order to mimic its dynamics. Since the same equations of motion hold for both systems, the solution of the underlying quantum problem is inferred by observing the time evolution of the artificially built model system while making use of its intrinsic quantumness. This scheme may be applied to the simulation of complex quantum problems, in the spirit originally proposed by Feynman [1].

Analog quantum simulation was previously performed to study fermionic transport [4] and magnetism [5] with cold atoms, while the exploration of non-equilibrium physics was proposed with an on-chip quantum simulator based on superconducting circuits [6, 7]. Digital simulation schemes with superconducting devices were demonstrated for fermionic models [8] and spin systems [9].

The quantum Rabi model in quantum optics describes the interaction between a two-level atom and a single quantized harmonic oscillator mode [10, 11]. In the weak coupling regime, which may still be strong in the sense of quantum electrodynamics (QED), a rotating wave ap-

proximation (RWA) can be applied and the Rabi model reduces to the Jaynes-Cummings model [12], which captures most relevant scenarios in cavity and circuit QED. In the ultra-strong coupling and the deep strong coupling regimes, where the coupling strength is comparable to the mode energies [13], the counter rotating terms in the interaction Hamiltonian can no longer be neglected and the RWA breaks down. As a consequence, the total excitation number in the quantum Rabi model is not conserved. Except for one recent paradigm of finding an exact solution [14], an analytically closed solution of the quantum Rabi model does not exist due to the lack of a second conserved quantity which renders it non-integrable. The quantum Rabi model, in particular in the ultra-strong coupling regime and beyond, exhibits non-classical features and rising interest in it is inspired by strong advances of experimental capabilities [13, 15–17]. The breakdown of the RWA in the ultra-strong coupling regime was previously observed with a superconducting circuit by implementing an increased physical coupling strength [18]. A similar approach involving a flux qubit coupled to a single-mode resonator allowed to access the deep strong coupling regime in a closed system [19]. The ultra-strong coupling regime was reached before by dynamically modulating the flux bias of a superconducting qubit, reaching a coupling strength of about 10% of the effective resonator frequency [20]. Here, we emulate the dynamics of the quantum Rabi model in the ultra-strong coupling regime with an analog quantum simulation scheme achieving a relative coupling strength of up to 0.7. With an alternative approach, the dynamics of the quantum Rabi model in ultra-strong coupling conditions was studied very recently [21].

Theory.— The quantum Rabi Hamiltonian reads

$$\hat{H}/\hbar = \frac{\epsilon}{2}\hat{\sigma}_z + \omega\hat{b}^\dagger\hat{b} + g\hat{\sigma}_x(\hat{b}^\dagger + \hat{b}), \quad (1)$$

with ϵ the qubit energy splitting, ω the bosonic mode frequency and g the transversal coupling strength. $\hat{\sigma}_i$ are Pauli matrices with $\hat{\sigma}_z|g\rangle = |g\rangle$ and $\hat{\sigma}_z|e\rangle = -|e\rangle$, where $|g\rangle$, $|e\rangle$ denote eigenstates of the computational qubit basis. \hat{b}^\dagger (\hat{b}) are creation (annihilation) operators in the Fock space of the bosonic mode. Both elements of the model are physically implemented in the experiment, with a small geometric coupling $g \ll \epsilon, \omega$, such that the RWA applies and Eq. (1) takes the form of the Jaynes-Cummings Hamiltonian. In order to access the ultra-strong coupling regime, we follow the scheme proposed in Ref. [22]. It is based on the application of two transversal microwave Rabi drive tones coupling to the qubit. The ultra-strong coupling condition is created in a synthesized effective Hamiltonian in the frame rotating with the dominant drive frequency. In this engineered Hamiltonian, the effective mode energies are set by the Rabi drive parameters. The Jaynes-Cummings Hamiltonian in the laboratory frame with both drives applied takes the form

$$\begin{aligned} \hat{H}/\hbar = & \frac{\epsilon}{2}\hat{\sigma}_z + \omega\hat{b}^\dagger\hat{b} + g(\hat{\sigma}_-\hat{b}^\dagger + \hat{\sigma}_+\hat{b}) \\ & + \hat{\sigma}_x\eta_1\cos(\omega_1t + \varphi_1) + \hat{\sigma}_x\eta_2\cos(\omega_2t + \varphi_2), \end{aligned} \quad (2)$$

with η_i the amplitudes and ω_i the frequencies of drive i . φ_i denotes the relative phase of drive i in the coordinate system of the qubit Bloch sphere in the laboratory frame. Within the RWA, the φ_i enter as relative phases of the transversal coupling operators $e^{-i\varphi_i}\hat{\sigma}_+ + \text{h.c.}$, where $\hat{\sigma}_\pm = 1/2(\hat{\sigma}_x \pm i\hat{\sigma}_y)$ denote Pauli's ladder operators. In the following, we set $\varphi_i = 0$ to recover the familiar $\hat{\sigma}_x$ coupling without loss of generality. Going to the frame rotating with ω_1 renders the first driving term time-independent, yielding

$$\begin{aligned} \hat{H}_1/\hbar = & (\epsilon - \omega_1)\frac{\hat{\sigma}_z}{2} + (\omega - \omega_1)\hat{b}^\dagger\hat{b} + g(\hat{\sigma}_-\hat{b}^\dagger + \hat{\sigma}_+\hat{b}) \\ & + \frac{\eta_1}{2}\hat{\sigma}_x + \frac{\eta_2}{2}\left(\hat{\sigma}_+e^{i(\omega_1-\omega_2)t} + \hat{\sigma}_-e^{-i(\omega_1-\omega_2)t}\right). \end{aligned} \quad (3)$$

The η_1 -term is now the significant term and we move into its interaction picture. Satisfying the requirement $\omega_1 - \omega_2 = \eta_1$ and applying a RWA yields the effective Hamiltonian in the ω_1 frame

$$\hat{H}_{\text{eff}}/\hbar = \frac{\eta_2}{2}\frac{\hat{\sigma}_z}{2} + \omega_{\text{eff}}\hat{b}^\dagger\hat{b} + \frac{g}{2}\hat{\sigma}_x(\hat{b}^\dagger + \hat{b}). \quad (4)$$

We define the effective bosonic mode energy $\omega_{\text{eff}} \equiv \omega - \omega_1$, which is the parameter governing the system dynamics. Noting $\eta_1 \gg \eta_2$, which is a necessary condition for the above approximation to hold, the effective qubit

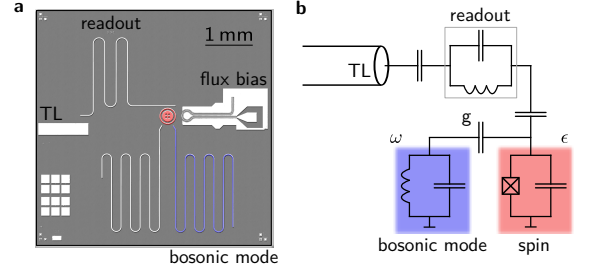


FIG. 1. Quantum simulation device. (a) Optical micrograph with the atomic spin represented by a concentric transmon qubit, highlighted in red and the $\lambda/2$ microstrip resonator (blue) constituting the bosonic oscillator mode. The readout resonator couples to the qubit capacitively and is read out with an open transmission line (TL) via the reflection signal of an applied microwave tone or pulse. The second resonator visible on chip is not used in the current experiment and is detuned in frequency from the relevant bosonic mode by ~ 0.5 GHz. (b) Effective circuit diagram of the device.

frequency η_2 and effective bosonic mode frequency ω_{eff} can be chosen as experimental parameters in the simulation. The complete coupling term of the quantum Rabi Hamiltonian is recovered, valid in the ultra-strong coupling regime and beyond, while the geometric coupling strength is only modified by a factor of two, resulting in $g_{\text{eff}} = g/2$. It is therewith feasible to tune the system into a regime where the coupling is similar or exceeds the effective mode energies. We want to point out that the coupling regime is defined by $g_{\text{eff}}/\omega_{\text{eff}}$, rather than involving the Rabi frequency η_1 , which does not enter the synthesized Hamiltonian. A detailed derivation of Eq. (4) can be found in Ref. [22] and is summarized in the Supplementary Material. The time evolution of the qubit measured in the laboratory frame is subject to fast oscillations corresponding to the Rabi frequency η_1 . Accordingly, the qubit dynamics in the engineered quantum Rabi Hamiltonian Eq. (4), valid in the ω_1 frame, can be inferred from the envelope of the evolution in the laboratory frame. A similar drive scheme based on a Rabi tone was previously used in experiment to synthesize an effective Hamiltonian with a rotated qubit basis [23].

Experimental methods.— The physical implementation of the quantum simulator is based on a superconducting circuit embedded in a typical circuit QED setup [24, 25], see Fig. 1. The atomic spin of the quantum Rabi model is mapped to a concentric transmon qubit [26, 27]. It is operated at a ratio of Josephson energy to charging energy $E_J/E_C = 50$ and an anharmonicity $\alpha/\hbar = \omega_{12}/2\pi - \omega_{01}/2\pi = -350 \text{ MHz} \sim E_C/\hbar = 306 \text{ MHz}$, close to resonance with the bosonic mode at 5.95 GHz. ω_{ij} denote the transition frequencies between transmon levels i, j . The inverse decay rate of the qubit at the operation point is measured to be $1/\Gamma_1 = 5 \mu\text{s}$. An on-chip flux bias line allows for a fast tuning of the qubit transition frequency as the concentric transmon is formed by a

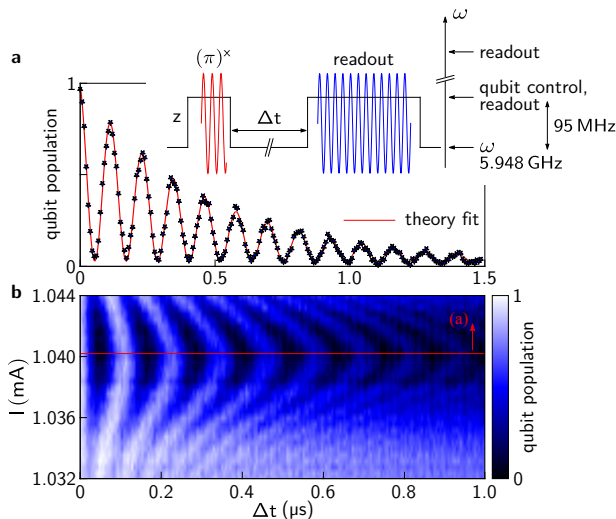


FIG. 2. Vacuum Rabi oscillations between qubit and bosonic mode. (a) The qubit is initially dc-biased on resonance with the bosonic mode, while it is detuned for state preparation and readout. The solid black line in the inset depicts the fast flux pulses applied to the flux bias line. A frequency fit (red) of the vacuum Rabi oscillations yields $2g/2\pi = 8.5$ MHz. The decay time $\Gamma^{-1} = 0.46$ μ s of the envelope is given by the mean of $1/T_1$ and κ . (b) For departing from the resonance condition (red line) by varying the dc bias current I , we observe the expected decrease in excitation swap efficiency and an increase in the vacuum Rabi frequency. The qubit population is given in colors and we applied a numerical interpolation of data points.

gradiometric dc-SQUID. The bosonic mode of the model is represented by a harmonic $\lambda/2$ resonator with a decay rate $\kappa/2\pi \sim 0.5$ MHz that is limited by capacitive coupling to the qubit. The sample fabrication process is detailed in the Supplemental Material.

The quantum circuit is mounted in an aluminum box and cooled to about 50 mK. It is enclosed in a cryoperm case for additional magnetic shielding. Qubit preparation and manipulation microwave pulses are generated by heterodyne single sideband mixing and applied to the same transmission line used for readout. In order to ensure phase control of the drive tones with respect to the qubit Bloch sphere coordinate system fixed by the first excitation pulse, we use a single microwave source for qubit excitation and the drives required by the simulation scheme. Different pulses are generated by heterodyne IQ mixing with separate IQ frequencies and amplitudes. The bosonic mode resonator is located far away from the transmission line which reduces parasitic driving. Readout of the qubit state is performed dispersively by means of a separate readout resonator located at 8.86 GHz in a projective measurement of the $\hat{\sigma}_z$ operator with a strong readout pulse of 400 ns duration. Further details on the experimental setup are given in the Supplemental Material.

Results.—The quantum state collapse followed by a quantum revival is the most striking signature of the ultra-strong and close deep strong coupling regime of the quantum Rabi model and emerges for qubit and bosonic mode being degenerate in the laboratory frame. We calibrate this resonance condition by minimizing the periodic swap rate of a single excitation between qubit and bosonic mode. Figure 2 shows the measured vacuum Rabi fluctuations in the resonant case (a) and dependent on the qubit transition frequency (b). For initial state preparation of the qubit and readout we detune the qubit by 95 MHz to a higher frequency. This corresponds to switching off the resonant interaction with the bosonic mode. Experimental details on flux pulse generation are described in the Supplemental Material. Rabi vacuum oscillations can be observed during the interaction time Δt and yield a coupling strength $g/2\pi = 4.3$ MHz, in agreement with the spectroscopically obtained result.

As the collapse-revival signature of the quantum Rabi model in ultra-strong coupling conditions manifests most clearly for a vanishing qubit term, we initially set $\eta_2 = 0$, yielding the effective Hamiltonian in the qubit frame

$$\hat{H}/\hbar = \omega_{\text{eff}} \hat{b}^\dagger \hat{b} + \frac{g}{2} \hat{\sigma}_x (\hat{b}^\dagger + \hat{b}). \quad (5)$$

Figure 3(a) shows the applied measurement sequence which is based on the one in Fig. 2 but extended by a drive tone of amplitude η_1 . The bosonic mode is initially in the vacuum state and the qubit is prepared in one of its basis states $|g\rangle, |e\rangle$, which are thermally impure. Qubit and bosonic mode are on resonance during the simulation time Δt , which is a necessary condition for the quantum revival to appear [28]. The drive is applied at a frequency ω_1 detuned from the common resonance point by ω_{eff} , setting the effective bosonic mode frequency in the rotating frame. Measured data for $\omega_{\text{eff}}/2\pi = 8$ MHz is displayed in Fig. 3(b), corresponding to $g_{\text{eff}}/\omega_{\text{eff}} \sim 0.3$. Stars show the experimentally simulated time evolution of the qubit prepared in $|e\rangle$. A fast quantum state collapse followed by periodically returning quantum revivals can be observed. The ground state of the qubit subspace in the driven system as well as in the synthesized Hamiltonian, Eq. (5), is in the equatorial plane of the qubit Bloch sphere and is assumed after a time $\Delta t \gg T_1, 1/\kappa$. It is diagonal in the $|\pm\rangle$ basis, with $|\pm\rangle = 1/\sqrt{2}(|e\rangle \pm |g\rangle)$. The revival dynamics can be understood with an intuitive picture in the laboratory frame. The eigenenergies in the $|\pm\rangle$ subspaces take the form of displaced vacuum

$$\omega_{\text{eff}} \left(\hat{b}^\dagger \pm \frac{g}{2\omega_{\text{eff}}} \right) \left(\hat{b} \pm \frac{g}{2\omega_{\text{eff}}} \right) + \text{const.}, \quad (6)$$

which is a coherent state that is not diagonal in the Fock basis. The prepared initial state in the experiment is therefore not an eigenstate in the effective basis with the drive applied such that many terms corresponding

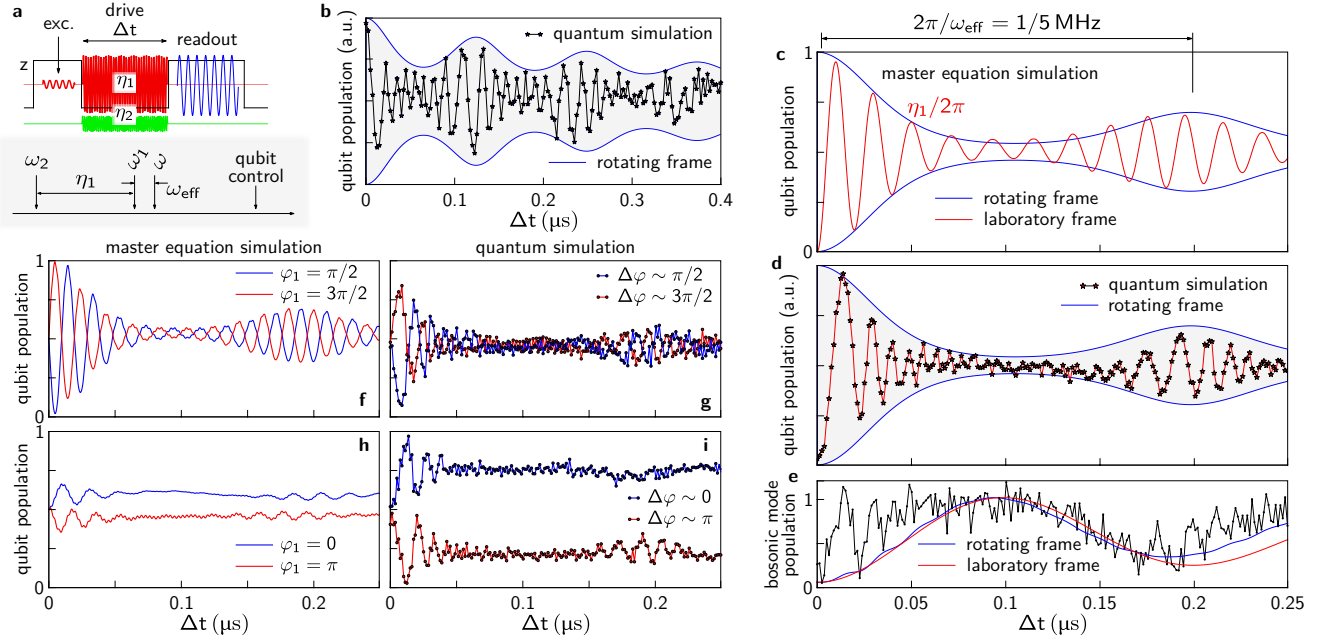


FIG. 3. Quantum state collapse and revival with only the dominant Rabi drive applied. (a) Schematic pulse sequence and overview on the relative frequencies used in the experiment. (b) Quantum simulation of the periodic recurrence of quantum state revivals for $\omega_{\text{eff}}/2\pi = 8$ MHz. The blue line corresponds to a master equation simulation of the qubit evolution in the rotating frame. (c), (d) Master equation and quantum simulation of the qubit time evolution for initial qubit states $|g\rangle$, $|e\rangle$ and $\omega_{\text{eff}}/2\pi = 5$ MHz, corresponding to $g_{\text{eff}}/\omega_{\text{eff}} \sim 0.5$. The red line shows the qubit population evolution of the driven system in the laboratory frame, Eq. (2), while the blue line follows the qubit evolution in the synthesized Hamiltonian Eq. (4). Experimental data shows the difference between two measurements for the qubit prepared in $|g\rangle$, $|e\rangle$, respectively, in order to isolate the qubit signal. (e) Measured population evolution of the bosonic mode, extracted from the sum of the two successive measurements, as compared to classically simulated data. (f)-(i) Qubit time evolution for varying relative phase φ_1 of the applied drive. The initial qubit state is prepared on the equator of the Bloch sphere $|g\rangle \pm |e\rangle$. Dispersive shifts induced by the bosonic mode are subtracted based on its classically simulated population evolution.

to the relevant Fock states n of the bosonic mode participate in the dynamics with phase factors $\exp\{in\omega_{\text{eff}}t\}$, $n \in \mathbb{N}^+$. While contributing terms get out of phase during the state collapse, they rephase after an idling period of $2\pi/\omega_{\text{eff}}$ to form the quantum revival [28]. The blue line in Fig. 3(b) corresponds to a classical master equation simulation of the qubit dynamics in the rotating frame in the two-level approximation. It includes the second excited level of the transmon [29] and decay terms in the underlying Liouvillian according to measured values. Refer to the Supplemental Material for further details. Figures 3(c),(d) show a classical simulation and the quantum simulation for $\omega_{\text{eff}}/2\pi = 5$ MHz with the qubit prepared in one of its eigenstates $|g\rangle$, $|e\rangle$. The population of the bosonic mode takes a maximum during the idling period and adopts its initial population at $2\pi/\omega_{\text{eff}}$ in the absence of dissipation, see Fig. 3(e). As evident from the maximum photon number in the bosonic mode, the excitation number is no longer a conserved quantity in the quantum Rabi model. Dependent on the coupling regime, we experimentally create entangled states involving up to three photons. By comparing simulated and measured data for varying ω_{eff} , we observe a differing effective decay enve-

lope of the quantum revivals. This reflects the varying total photon number in the system which is proportional to the ratio g/ω_{eff} . The fast oscillations in Fig. 3(c), (d) correspond to the Rabi frequency $\eta_1/2\pi \sim 50$ MHz, as extracted from Fourier transformation of measured data.

While the phase of the qubit Bloch vector is not well defined for initial states $|g\rangle$, $|e\rangle$, the qubit state carries phase information when prepared on the equatorial plane of the Bloch sphere via a $\pi/2$ pulse. Figures 3(f)-(i) show the qubit time evolution with varying relative phase φ_1 between initial state and applied drive, plotted in the original qubit basis, as calibrated in a Rabi oscillation experiment. Experimentally, the orientation of the coordinate system is set by the first microwave pulse and we apply the Rabi drive with a varying relative phase φ_1 , corresponding to the angle between qubit Bloch vector and rotation axis of the drive in the equatorial plane. When both are perpendicular, $\varphi_1 = \pm\pi/2$, similar oscillations including the state revival can be observed, assuming a steady state in the equatorial plane. For the case where $\varphi_1 = 0, \pi$, qubit oscillations in the laboratory frame are suppressed while the baseline is shifted up or down due to the detuning of the Rabi drive. The

substructure emerges from the swap interaction term between qubit and bosonic mode that may be regarded as a perturbation as $\eta_1 \gg g$. Classical master equation simulations confirm that the basis shift, dependent on the prepared initial qubit state, is enhanced by the presence of the second excited transmon level and by a spectral broadening of the applied Rabi drive. The experimentally observed shift is not entirely captured by the classical simulation which we attribute to missing higher order terms in the master equation. Dependent on φ_1 we likewise observe a varying maximum photon population of the bosonic mode in classical simulations and indicated in the dispersive shift of the readout resonator. A deviation of the effective qubit basis is likewise observed for preparing the qubit in one of its eigenstates $|g\rangle$, $|e\rangle$.

In measuring the dispersive shift of the readout resonator during the experiment in Fig. 3, we observe a bulged and shifted equatorial baseline following the population evolution of the bosonic mode as obtained from the master equation simulation. By simulating the full circuit Hamiltonian including qubit, bosonic mode and readout resonator with all mutual coupling terms, we find an additional cross-Kerr coupling λ between the bosonic mode and the readout resonator. This becomes feasible as the bosonic mode inherits nonlinearity from the qubit, required for inducing a photon number dependent shift on a harmonic mode. In Fig. 3(d) we made use of the topological symmetry of simulations with initial qubit states $|g\rangle$, $|e\rangle$, by subtracting two successive measurements with the qubit prepared in its eigenstates $|g\rangle$, $|e\rangle$, respectively, in order to cancel out the additional dispersive shift induced by the bosonic mode. Due to a lack of such a symmetry, the qubit population as depicted in Fig. 3(f-i) is retrieved from measured raw data by subtracting the classically simulated dispersive shift induced by the bosonic mode. Here, the dispersive shift $\propto \lambda^2$ remains as the only free fit parameter and qualitatively agrees with the one extracted from measured data, see the Supplemental Material. Likewise, we obtain the population evolution of the bosonic mode, depicted in Fig. 3(e), by summing two successive measurements with the qubit prepared in $|g\rangle$, $|e\rangle$, respectively. The additional cross-Kerr λ therefore provides indirect access to the population of the bosonic mode without a dedicated readout device available.

The validity of the analog simulation scheme proposed in Ref. [22] and used in this letter is confirmed by simulations presented in the Supplemental Material. We demonstrate that the dynamics of the qubit and the bosonic mode in the quantum Rabi model is well reproduced by the constructed effective Hamiltonian and that the population of the bosonic mode is independent of the Rabi drive amplitude η_1 , despite of it forming a large energy reservoir that is provided to the circuit.

In order to simulate the full quantum Rabi model including a non-vanishing qubit energy term we switch on

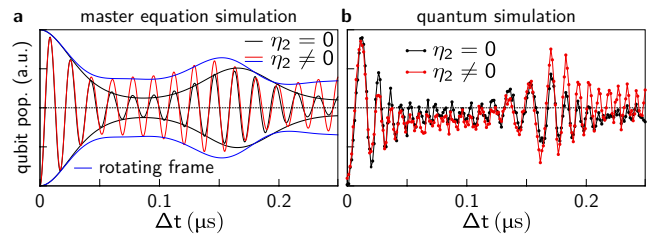


FIG. 4. Simulation of the full quantum Rabi model. (a) Master equation simulations for vanishing qubit term $\eta_2 = 0$ (black) and with non-vanishing qubit term $\eta_2 > 0$ (red). The blue line corresponds to the classical simulation for $\eta_2/2\pi = 3$ MHz. (b) Quantum simulation for equal parameters. The dispersive shift of the readout resonator induced by the bosonic mode is subtracted based on classically simulated data.

the second drive, $\eta_2 \neq 0$. Quantum simulations are performed with the qubit initially in $|g\rangle$, subject to thermal excess population. The drive tones are up-converted in two separate IQ mixers while sharing a common local oscillator input to preserve their relative phase relation. For the simulation scheme to be valid, we need to fulfill the constraint $\omega_2 = \omega_1 - \eta_1$. This is achieved by initially applying a simulation sequence with $\eta_2 = 0$ in order to obtain the frequency equivalent of the Rabi frequency η_1 from a Fourier transformation of the qubit time evolution. Subsequently, we apply the same sequence with a finite η_2 , $\varphi_1 = \varphi_2$ and ω_2 set by obeying the above constraint. Figure 4 shows classical simulation (a) and quantum simulation (b) of the complete quantum Rabi model for $\eta_2 = 0$ (black) and $\eta_2 \neq 0$ (red). Measured data deviates from the expectation for short Δt in particular, which we attribute to the spectral broadening of the weak Rabi drive. However, we observe a significant increase in the revival amplitude as well as more pronounced oscillations after the first revival, in agreement with the classical simulation. These signatures vanish for departing from the above constraint or applying the weak Rabi drive with a phase delay $\varphi_1 \neq \varphi_2$, see Supplemental Material. We estimate the frequency equivalent of $\eta_2/2\pi \sim 3$ MHz via comparing the relative peak heights of both drive tones with a spectrum analyzer. With $\omega_{\text{eff}} = 6$ MHz we approach a regime where $2g_{\text{eff}}/\sqrt{\omega_{\text{eff}}\eta_2/2} > 1$.

Conclusion.— We have demonstrated analog quantum simulation of the full quantum Rabi model in the ultra-strong and close deep strong coupling regime. The distinct quantum state collapse and revival signature in the qubit dynamics was observed, validating the experimental feasibility of the proposed scheme [22]. The main limitation of the approach is the small anharmonicity α of the transmon which limits Rabi frequencies to about $100 \text{ MHz} \sim 0.3\alpha$, in order to avoid higher level population. In addition, a parasitic coupling of the applied drives to the bosonic mode gives rise to an excess pop-

ulation of the bosonic mode that eventually limits the simulation quality. The coupling regime is limited by our circuit's coherence such that an entangled state can be preserved until the onset of the first revival for a coupling regime where $g_{\text{eff}}/\omega_{\text{eff}} \sim 0.7$. The scheme may be a route to efficiently generate non-classical cavity states [30–32]. Based on the demonstrated phase control on the microwave drives, the simulation scheme may be extended to explore physical models such as the Dirac equation in (1+1) dimensions. Its characteristic dynamics is expected to display a *Zitterbewegung* in the spacial quadrature of the bosonic mode [22].

It has been shown recently that a quantum phase transition, typically requiring a continuum of modes, can appear already in the quantum Rabi model under appropriate conditions [33]. The experimental challenge is projected to the coupling requirements in the model which may be accomplished with the simulation scheme presented. This can be a starting point to experimentally investigate critical phenomena in a small and well-controlled quantum system [34]. While the presented dynamics can still be efficiently simulated on a classical computer, a true quantum supremacy will onset when incorporating more modes. Substituting the single quantized mode by a continuous bosonic bath renders our setup a viable tool for investigating the spin boson model in various coupling regimes, which recently attracted experimental interest in the context of quantum simulations [35, 36]. The presented simulation scheme can be applied for a continuum of modes, such that an engineered bath in a restricted frequency band is collectively shifted by the applied Rabi frequency. This can become a route to address the infrared cutoff issue in a tailored bosonic bath and to observe quantum phase transitions in the spin boson model.

The authors acknowledge valuable discussions with G. Romero, M.-J. Hwang, I. Pop, U. Vool, J. Pedernales and E. Solano. We are grateful to L. Radtke and S. Diewald for support during sample fabrication and A. Lukashenko for assistance in cryostat operation. This work was supported by the European Research Council (ERC) within consolidator grant No. 648011 and through the KIT Nanostructure Service Laboratory (NSL). This work was also supported in part by the Ministry for Education and Science of the Russian Federation via NUST MISIS under contracts K2-2015-002 and K2-2016-051. J.B. acknowledges financial support by the Landesgraduiertenförderung (LGF) of the federal state Baden-Württemberg. A.Sch. acknowledges financial support by the Carl-Zeiss-Foundation.

* jochen.braumueller@kit.edu.

[1] R. P. Feynman, Int. J. Theor. Phys. **21**, 467 (1982).

- [2] S. Lloyd, Science **273**, 1073 (1996).
- [3] I. M. Georgescu, S. Ashhab, and F. Nori, Rev. Mod. Phys. **86**, 153 (2014).
- [4] U. Schneider, L. Hackermüller, J. P. Ronzheimer, S. Will, S. Braun, T. Best, I. Bloch, E. Demler, S. Mandt, D. Rasch, and A. Rosch, Nat. Phys. **8**, 213 (2012).
- [5] D. Greif, T. Uehlinger, G. Jotzu, L. Tarruell, and T. Esslinger, Science **340**, 1307 (2013).
- [6] A. A. Houck, H. E. Türeci, and J. Koch, Nat. Phys. **8**, 292 (2012).
- [7] J.-M. Reiner, M. Marthaler, J. Braumüller, M. Weides, and G. Schön, Phys. Rev. A **94**, 032338 (2016).
- [8] R. Barends, L. Lamata, J. Kelly, L. García-Álvarez, A. G. Fowler, A. Megrant, E. Jeffrey, T. C. White, D. Sank, J. Y. Mutus, B. Campbell, Y. Chen, Z. Chen, B. Chiaro, A. Dunsworth, I.-C. Hoi, C. Neill, P. J. J. O'Malley, C. Quintana, P. Roushan, A. Vainsencher, J. Wenner, E. Solano, and J. M. Martinis, Nat. Commun. **6**, 7654 (2015).
- [9] Y. Salathé, M. Mondal, M. Oppliger, J. Heinsoo, P. Kurpiers, A. Potocnik, A. Mezzacapo, U. Las Heras, L. Lamata, E. Solano, S. Filipp, and A. Wallraff, Phys. Rev. X **5**, 021027 (2015).
- [10] I. I. Rabi, Phys. Rev. **49**, 324 (1936).
- [11] I. I. Rabi, Phys. Rev. **51**, 652 (1937).
- [12] E. Jaynes and F. Cummings, Proc. IEEE **51**, 89 (1963).
- [13] J. Casanova, G. Romero, I. Lizuain, J. J. García-Ripoll, and E. Solano, Phys. Rev. Lett. **105**, 263603 (2010).
- [14] D. Braak, Phys. Rev. Lett. **107**, 100401 (2011).
- [15] S. Ashhab and F. Nori, Phys. Rev. A **81**, 042311 (2010).
- [16] F. Beaudoin, J. M. Gambetta, and A. Blais, Phys. Rev. A **84**, 043832 (2011).
- [17] C. H. Alderete and B. M. Rodríguez-Lara, (2016), 1604.04012.
- [18] T. Niemczyk, F. Deppe, H. Huebl, E. P. Menzel, F. Hocke, M. J. Schwarz, J. J. García-Ripoll, D. Zueco, T. Hümmer, E. Solano, A. Marx, and R. Gross, Nat. Phys. **6**, 772 (2010).
- [19] F. Yoshihara, T. Fuse, S. Ashhab, K. Kakuyanagi, S. Saito, and K. Semba, Nat. Phys. (2016), 10.1038/nphys3906.
- [20] J. Li, M. Silveri, K. Kumar, J.-M. Pirkkalainen, A. Vepsäläinen, W. Chien, J. Tuorila, M. Sillanpää, P. Hakonen, E. Thuneberg, and et al., Nat. Commun. **4**, 1420 (2013).
- [21] N. K. Langford, R. Sagastizabal, M. Kounalakis, C. Dickel, A. Bruno, F. Luthi, D. J. Thoen, A. Endo, and L. DiCarlo, (2016), arXiv1610.10065.
- [22] D. Ballester, G. Romero, J. J. García-Ripoll, F. Deppe, and E. Solano, Phys. Rev. X **2**, 021007 (2012).
- [23] U. Vool, S. Shankar, S. O. Mundhada, N. Ofek, A. Narla, K. Sliwa, E. Zaly-Geller, Y. Liu, L. Frunzio, R. J. Schoelkopf, S. M. Girvin, and M. H. Devoret, Phys. Rev. Lett. **117**, 133601 (2016).
- [24] A. Blais, R.-S. Huang, A. Wallraff, S. M. Girvin, and R. J. Schoelkopf, Phys. Rev. A **69**, 062320 (2004).
- [25] A. Wallraff, D. I. Schuster, A. Blais, L. Frunzio, R.-S. Huang, J. Majer, S. Kumar, S. M. Girvin, and R. J. Schoelkopf, Nature **431**, 162 (2004).
- [26] J. Koch, T. M. Yu, J. Gambetta, A. A. Houck, D. I. Schuster, J. Majer, A. Blais, M. H. Devoret, S. M. Girvin, and R. J. Schoelkopf, Phys. Rev. A **76**, 042319 (2007).
- [27] J. Braumüller, M. Sandberg, M. R. Vissers, A. Schneider,

- S. Schlör, L. Grünhaupt, H. Rotzinger, M. Marthaler, A. Lukashenko, A. Dieter, A. V. Ustinov, M. Weides, and D. P. Pappas, *Appl. Phys. Lett.* **108**, 032601 (2016).
- [28] S. Haroche and J.-M. Raimond, *Exploring the Quantum - Atoms, Cavities, and Photons* (Oxford University Press, 2006).
- [29] J. Braumüller, J. Cramer, S. Schlör, H. Rotzinger, L. Radtke, A. Lukashenko, P. Yang, S. T. Skacel, S. Probst, M. Marthaler, L. Guo, A. V. Ustinov, and M. Weides, *Phys. Rev. B* **91**, 054523 (2015).
- [30] Z. Leghtas, S. Touzard, I. M. Pop, A. Kou, B. Vlastakis, A. Petrenko, K. M. Sliwa, A. Narla, S. Shankar, M. J. Hatridge, M. Reagor, L. Frunzio, R. J. Schoelkopf, M. Mirrahimi, and M. H. Devoret, *Science* **347**, 853 (2015).
- [31] G. Kirchmair, B. Vlastakis, Z. Leghtas, S. E. Nigg, H. Paik, E. Ginossar, M. Mirrahimi, L. Frunzio, S. M. Girvin, and R. J. Schoelkopf, *Nature* **495**, 205 (2013).
- [32] B. Vlastakis, G. Kirchmair, Z. Leghtas, S. E. Nigg, L. Frunzio, S. M. Girvin, M. Mirrahimi, M. H. Devoret, and R. J. Schoelkopf, *Science* **342**, 607 (2013).
- [33] M.-J. Hwang, R. Puebla, and M. B. Plenio, *Phys. Rev. Lett.* **115**, 180404 (2015).
- [34] M.-J. Hwang and M. B. Plenio, (2016), arXiv1603.03943.
- [35] M. Haeberlein, F. Deppe, A. Kurcz, J. Goetz, A. Baust, P. Eder, K. Fedorov, M. Fischer, E. P. Menzel, M. J. Schwarz, F. Wulschner, E. Xie, L. Zhong, E. Solano, A. Marx, J.-J. Garca-Ripoll, and R. Gross, (2015), arXiv1506.09114.
- [36] P. Forn-Díaz, J. J. Garca-Ripoll, B. Peropadre, J. L. Orgiazzi, M. A. Yurtalan, R. Belyansky, C. M. Wilson, and A. Lupascu, *Nat. Phys.* (2016), 10.1038/nphys3905.

Analog quantum simulation of the Rabi model in the ultra-strong coupling regime Supplemental Material

Jochen Braumüller,^{1,*} Michael Marthaler,² Andre Schneider,¹ Alexander
Stehli,¹ Hannes Rotzinger,¹ Martin Weides,^{1,3} and Alexey V. Ustinov^{1,4}

¹*Physikalisches Institut, Karlsruhe Institute of Technology, 76131 Karlsruhe, Germany*

²*Institut für Theoretische Festkörperphysik, Karlsruhe Institute of Technology, 76131 Karlsruhe, Germany*

³*Physikalisches Institut, Johannes Gutenberg University Mainz, 55128 Mainz, Germany*

⁴*Russian Quantum Center, National University of Science and Technology MISIS, Moscow 119049, Russia*

(Dated: November 28, 2016)

THEORETICAL BASICS OF THE SIMULATION SCHEME

The simulation scheme we detail here follows a proposal published in Ref. [S1]. The quantum Rabi Hamiltonian to be constructed reads

$$\hat{H}/\hbar = \frac{\epsilon}{2}\hat{\sigma}_z + \omega\hat{b}^\dagger\hat{b} + g\hat{\sigma}_x(\hat{b}^\dagger + \hat{b}), \quad (\text{S1})$$

with ϵ the qubit energy splitting, ω the resonator frequency and g the transversal coupling strength. $\hat{\sigma}_i$ are Pauli matrices with $\hat{\sigma}_z|g\rangle = |g\rangle$ and $\hat{\sigma}_z|e\rangle = -|e\rangle$, where $|g\rangle$ and $|e\rangle$ are the qubit groundstate and first excited state, respectively. We neglect the qubit tunneling matrix element Δ such that the qubit Hamiltonian remains

$$\hat{H}_q = \frac{\epsilon}{2}\hat{\sigma}_z + \frac{\Delta}{2}\hat{\sigma}_x \approx \frac{\epsilon}{2}\hat{\sigma}_z. \quad (\text{S2})$$

$\Delta \ll \epsilon$ is valid for the transmon qubit within the WKB approximation [S2]. \hat{b}^\dagger (\hat{b}) are creation (annihilation) operators in the resonator Fock space. Throughout this derivation, operators acting on either the qubit or the resonator subspace of the joint Hilbert space are written without the formally correct tensor product with the unity in the other subspace, such that $\mathbb{1}_2 \otimes \hat{b}^\dagger\hat{b} \equiv \hat{b}^\dagger\hat{b}$, $\hat{\sigma}_z \otimes \mathbb{1}_r \equiv \hat{\sigma}_z$. $\mathbb{1}_2$ denotes unity in the qubit Hilbert space while $\mathbb{1}_r$ denotes unity in the bosonic mode Hilbert space of dimension r . Likewise, the tensor product symbol is omitted for clarity.

The qubit and the bosonic oscillator mode are physical elements of the quantum simulator implemented on chip. Since the geometric coupling g on chip is small compared to the mode energies, $g/\epsilon \ll 1$ and $g/\omega \ll 1$, the rotating wave approximation (RWA) is valid and Eq. (S1) takes the form of the Jaynes-Cummings Hamiltonian [S3]. The construction of the effective Hamiltonian relies on the application of two transversal microwave tones acting on the qubit. The key feature is a renormalization of the mode energies ϵ , ω by experimental parameters in the frame rotating with the first dominant drive. Even though a RWA may be used to simplify the ordinary Jaynes-Cummings Hamiltonian as implemented on chip, the RWA breaks down for the quantum Rabi Hamiltonian in the ultra-strong coupling regime and beyond. Therefore the complete coupling term $g\hat{\sigma}_x(\hat{b}^\dagger + \hat{b})$ needs to be preserved. The Jaynes-Cummings Hamiltonian in the laboratory frame with the two drives applied takes the form

$$\hat{H}/\hbar = \frac{\epsilon}{2}\hat{\sigma}_z + \omega\hat{b}^\dagger\hat{b} + g(\hat{\sigma}_-\hat{b}^\dagger + \hat{\sigma}_+\hat{b}) + \hat{\sigma}_x\eta_1 \cos(\omega_1 t + \varphi_1) + \hat{\sigma}_x\eta_2 \cos(\omega_2 t + \varphi_2),$$

with η_i the amplitudes, ω_i the frequencies and φ_i the relative phase of drive i . In the following derivation we set $\varphi_i = 0$ without loss of generality. We use Pauli's ladder operators $\hat{\sigma}_\pm = 1/2(\hat{\sigma}_x \pm i\hat{\sigma}_y)$. The unitary transformation \hat{U} for changing into the frame rotating with the dominant drive η_1 reads

$$\hat{U} = \exp \left\{ i\omega_1 t \left(\hat{b}^\dagger\hat{b} + \frac{1}{2}\hat{\sigma}_z \right) \right\}. \quad (\text{S3})$$

Performing the transformation $|\tilde{\psi}\rangle = U|\psi\rangle$ of eigenstates $|\psi\rangle$ leads to a transformed Hamiltonian \tilde{H} according to

$$\tilde{H} = \hat{U}\hat{H}\hat{U}^\dagger - i\hat{U}\dot{\hat{U}}^\dagger. \quad (\text{S4})$$

The transformation of Eq. (S3) yields

$$\begin{aligned} \tilde{H} = & \frac{\epsilon}{2}\hat{\sigma}_z + \omega\hat{b}^\dagger\hat{b} + g(\hat{\sigma}_+e^{i\omega_1 t} + \hat{\sigma}_-e^{-i\omega_1 t})(e^{i\omega_1 t}\hat{b}^\dagger + e^{-i\omega_1 t}\hat{b}) \\ & + \eta_1(\hat{\sigma}_+e^{i\omega_1 t} + \hat{\sigma}_-e^{-i\omega_1 t})\cos\omega_1 t + \eta_2(\hat{\sigma}_+e^{i\omega_1 t} + \hat{\sigma}_-e^{-i\omega_1 t})\cos\omega_2 t - \omega_1\left(\hat{b}^\dagger\hat{b} + \frac{1}{2}\hat{\sigma}_z\right) \end{aligned} \quad (\text{S5})$$

$$\begin{aligned} = & \frac{1}{2}(\epsilon - \omega_1)\hat{\sigma}_z + (\omega - \omega_1)\hat{b}^\dagger\hat{b} + g(\hat{\sigma}_-\hat{b}^\dagger + \hat{\sigma}_+\hat{b}) + \frac{\eta_1}{2}(\hat{\sigma}_+ + \hat{\sigma}_-) + \frac{\eta_2}{2}(\hat{\sigma}_+e^{i(\omega_1-\omega_2)t} + \hat{\sigma}_-e^{-i(\omega_1-\omega_2)t}) \\ & + g(\hat{\sigma}_+e^{2i\omega_1 t}\hat{b}^\dagger + \hat{\sigma}_-e^{-2i\omega_1 t}\hat{b}) + \frac{\eta_1}{2}(\hat{\sigma}_+e^{2i\omega_1 t} + \hat{\sigma}_-e^{-2i\omega_1 t}) + \frac{\eta_2}{2}(\hat{\sigma}_+e^{i(\omega_1+\omega_2)t} + \hat{\sigma}_-e^{i(-\omega_1-\omega_2)t}). \end{aligned} \quad (\text{S6})$$

Terms of the form $e^X Y e^{-X}$ are calculated using the power series expansion of the exponential function, also called Hadamard lemma. For $X = i\omega_1 t \hat{b}^\dagger\hat{b}$, $Y = \hat{b}^\dagger$,

$$e^{i\omega_1 t \hat{b}^\dagger\hat{b}} \hat{b}^\dagger e^{-i\omega_1 t \hat{b}^\dagger\hat{b}} = e^{i\omega_1 t} \hat{b}^\dagger \quad (\text{S7})$$

$$e^{i\omega_1 t \hat{b}^\dagger\hat{b}} \hat{b} e^{-i\omega_1 t \hat{b}^\dagger\hat{b}} = e^{-i\omega_1 t} \hat{b} \quad (\text{S8})$$

since

$$\sum_{m=0}^{\infty} \frac{1}{m!} \left[i\omega_1 t \hat{b}^\dagger \hat{b}, \hat{b}^\dagger \right]_m = \hat{b}^\dagger \sum_{m=0}^{\infty} \frac{1}{m!} (i\omega_1 t)^m = \hat{b}^\dagger e^{i\omega_1 t}. \quad (\text{S9})$$

$e^{\frac{i}{2}\omega_1 t \hat{\sigma}_z}$ and $\hat{\sigma}_z$ clearly commute, while

$$e^{\frac{i}{2}\omega_1 t \hat{\sigma}_z} \hat{\sigma}_x e^{-\frac{i}{2}\omega_1 t \hat{\sigma}_z} = \hat{\sigma}_+ e^{i\omega_1 t} + \hat{\sigma}_- e^{-i\omega_1 t} \quad (\text{S10})$$

using $e^{\text{diag}(a,b)} = \text{diag}(e^a, e^b)$. Terms in the last line in Eq. (S6) are omitted in the following within the RWA, valid for $\eta_1/2\omega_1 \ll 1$. This is always a good approximation as η_1 is bound in the experiment by the qubit anharmonicity $|\alpha| \lesssim 350$ MHz.

The η_1 term in the transformed Hamiltonian Eq. (S6) is the most significant term, which justifies to move to its interaction picture. Under the constraint $\eta_1 \equiv \omega_1 - \omega_2$, the Hamiltonian in the interaction picture becomes

$$\begin{aligned} e^{i\frac{\eta_1}{2}\hat{\sigma}_x t} \left[\tilde{H} - \frac{\eta_1}{2}\hat{\sigma}_x \right] e^{-i\frac{\eta_1}{2}\hat{\sigma}_x t} &= \frac{\eta_2}{2} \begin{pmatrix} \sin^2 \eta_1 t & \cos \eta_1 t + i \sin 2\eta_1 t \\ \cos \eta_1 t - i \sin 2\eta_1 t & -\sin^2 \eta_1 t \end{pmatrix} \\ &+ \frac{1}{2}(\epsilon - \omega_1) \begin{pmatrix} \cos \eta_1 t & -i \sin \eta_1 t \\ i \sin \eta_1 t & -\cos \eta_1 t \end{pmatrix} + (\omega - \omega_1) \hat{b}^\dagger \hat{b} \\ &+ g \left[\begin{pmatrix} -\frac{1}{2}i \sin \eta_1 t & \frac{1}{2}(1 + \cos \eta_1 t) \\ \frac{1}{2}(1 - \cos \eta_1 t) & \frac{1}{2}i \sin \eta_1 t \end{pmatrix} \hat{b}^\dagger + \begin{pmatrix} \frac{1}{2}i \sin \eta_1 t & \frac{1}{2}(1 - \cos \eta_1 t) \\ \frac{1}{2}(1 + \cos \eta_1 t) & -\frac{1}{2}i \sin \eta_1 t \end{pmatrix} \hat{b} \right]. \end{aligned} \quad (\text{S11})$$

Neglecting again time dependent terms in the spirit of a RWA casts Eq. (S11) into the desired form of the quantum Rabi Hamiltonian

$$\hat{H}_{\text{eff}}/\hbar = \frac{\eta_2}{2} \frac{\hat{\sigma}_z}{2} + \omega_{\text{eff}} \hat{b}^\dagger \hat{b} + \frac{g}{2} \sigma_x (\hat{b}^\dagger + \hat{b}), \quad (\text{S12})$$

with $\omega_{\text{eff}} \equiv \omega - \omega_1$ and noting that $\eta_1 \gg \eta_2$.

SAMPLE FABRICATION

Sample fabrication was carried out in one single electron beam lithography step. The Josephson junctions are formed by shadow angle evaporation and a Dolan bridge technique with electrode film thicknesses of 30 nm and 50 nm, respectively, resulting in a Al film thickness of 80 nm across the entire chip. The area of the Josephson junctions is designed to be $100 \text{ nm} \times 220 \text{ nm}$, resulting in a critical current $I_c = 45 \text{ nA}$ for a single junction. Al is evaporated at a chamber background pressure of about 3×10^{-8} mbar. We applied an Al metalization on the backside of the double-side polished intrinsic Si substrate as a ground reference for the microstrip elements on chip. Electric field coupling in the substrate due to the backside metalization accounts for roughly half of the qubit capacitance [S4].

EXPERIMENTAL SETUP

Microwave setup

The schematic diagram of the measurement and microwave setup is depicted in Fig. S1. We readout the qubit state by observing a dispersive shift of the readout resonator which is acquired via a 400 ns long readout pulse. The resonator shift is extracted from the microwave reflection signal at a single-ended 50Ω matched transmission line that capacitively couples to the readout resonator. We down-convert the readout pulse by heterodyne single sideband mixing to eliminate parasitic population of the readout device during pulse-off time.

Qubit excitation and Rabi driving are performed by heterodyne mixing with respective IQ frequencies for different drive and excitation frequencies, using one single microwave source and one IQ mixer, see Fig. S1(a). This allows for the required phase control on the phases φ_1, φ_2 of the Rabi drives. In particular, we fix the idling time between initial

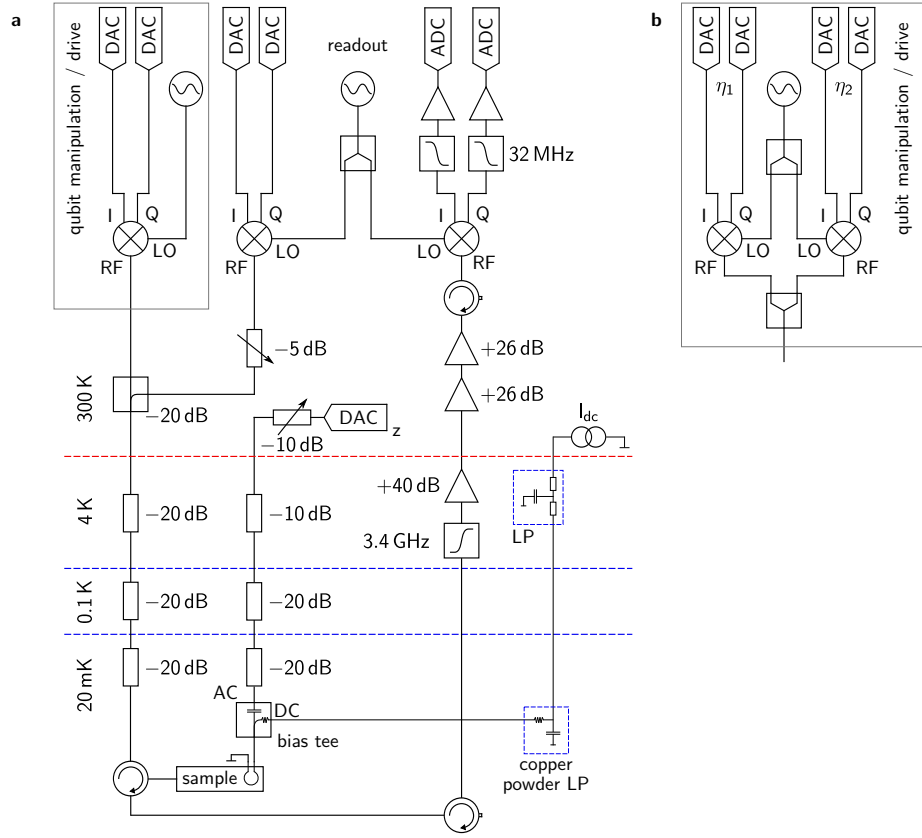


FIG. S1. (a) Schematic microwave setup used for the quantum simulation experiment. (b) Modification of the microwave setup (substituting the gray rectangle) for the application of two drive pulses with amplitudes η_1, η_2 . The drive pulses are generated with two separate IQ mixers, sharing a common local oscillator (LO) input, and combined subsequently.

excitation pulse and the onset of the Rabi drive, such that the acquired phase during that time is constant, and apply the Rabi drive(s) with a constant relative phase φ_i with respect to the phase used for the excitation pulse. We chose an LO frequency located 20 MHz or 65 MHz above the qubit excitation and readout frequency. In the experiment with the second Rabi drive added, we generate the drives initially in separate IQ mixers that share a common LO input. We suppress phase errors by employing identical coaxial cables for the high-frequency lines prior to the combination of the drive pulses. The microwave pulses for $\hat{X}\hat{Y}$ control of the qubit are applied via the same transmission line used for readout.

The qubit transition frequency is adjusted by a dc current applied to the on-chip flux coil. High frequency noise is filtered at the 4 K stage with RCR type π -filters at about 25 kHz and on the base plate via an RC-element enclosed in copper powder [S5]. Fast flux pulses for fast \hat{Z} pulsing of the qubit are sent through a separate microwave line and combined with the offset current by means of a bias tee located at the base plate.

Compensation for finite bias tee time constant

In order to combine dc and ac flux signals that are applied to the flux bias line without breaking the 50Ω impedance matching, we make use of a bias tee in the experiment. Due to a finite time constant τ of the bias tee, a continuous compensation for discharging effects is required in order to produce the desired pulse sequence in the flux bias line on chip. Figure S2(a) shows the schematic circuit diagram present during flux pulse generation. V_{ex} denotes the amplitude of the voltage pulse, R is the line resistance in front of the bias tee and C is the relevant capacitance of the bias tee. From Kirchhoff's law we can write

$$RI + \frac{Q}{C} = V_{ex}, \quad (\text{S13})$$

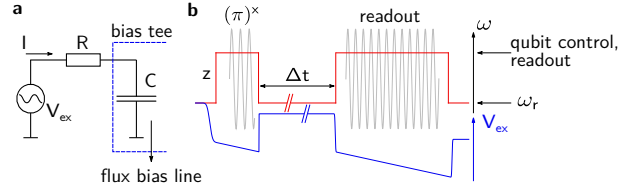


FIG. S2. (a) Schematic circuit diagram prevailing flux pulse generation. Microwave pulses of amplitude V_{ex} pass a resistor R and charge the capacitor which is part of the bias tee. (b) Due to the finite time constant τ of the bias tee, voltage pulses of amplitude V_{ex} following the blue line are applied to its input such that the resulting flux through the on chip flux coil follows the ideal pulse sequence depicted in red.

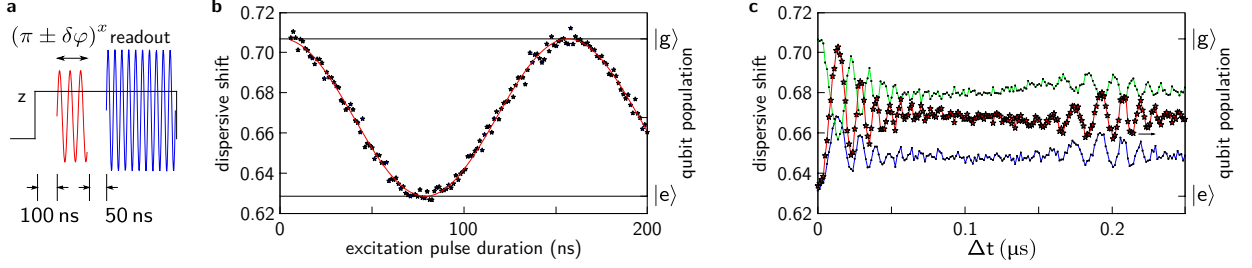


FIG. S3. Calibration of the qubit basis with a Rabi experiment using the z pulsing sequence used in the simulation experiment. (a) Schematic pulse sequence used for the calibration. Qubit and bosonic mode are on resonance initially. A fast flux pulse is applied to tune the qubit out of resonance for excitation and readout. The length of the excitation pulse corresponding to the rotation angle φ around the Bloch sphere is varied during the calibration. (b) Qubit Rabi oscillations with a sinusoidal fit (red). We identify the computational qubit basis spanned by the groundstate $|g\rangle$ and the first excited state $|e\rangle$. (c) Dispersive shift of the readout resonator for a simulation sequence with $\omega_{eff}/2\pi = 5$ MHz and the qubit prepared in either $|e\rangle$ (blue) or $|g\rangle$ (green). The faintly visible bulge cancels by evaluating their difference, plotted in red.

with I the current that is admitted to the flux bias line. The condition of constant current follows from requesting

$$\frac{dI}{dt} = \frac{1}{R} \frac{dV_{ex}}{dt} - \frac{1}{RC} I \stackrel{!}{=} 0, \quad (\text{S14})$$

which yields

$$\frac{d}{dt} V_{ex} = \frac{I}{C}. \quad (\text{S15})$$

Since I is not a function of time according to the initial claim, Eq. (S15) can be integrated yielding

$$V_{ex} = \frac{1}{C} I t + \text{const.} \propto t. \quad (\text{S16})$$

This shows that the required correction of the externally applied voltage V_{ex} is linear in time t with a slope proportional to $1/\tau$. See the pulse sequence applied (blue) and the resulting pattern (red) in Fig. S2(b). During pulse-off time, V_{ex} has to be kept constant and no further correction is required. The utilized pulse sequence therefore scales nicely for perspective longer simulation times since the described compensation can be performed for not longer than approximately $1 \mu\text{s}$ within one continuous pulse sequence.

We calibrated the time constant of the bias tee used in the experiment to be $\tau = 0.7 \mu\text{s}$.

CALIBRATION OF THE QUBIT BASIS AND BASELINE SHIFT

Calibration of the qubit basis

Prior to the experiments presented in the main text, we calibrated the qubit basis spanned by eigenstates $|g\rangle$, $|e\rangle$. This is of relevance for the data analysis detailed in Sec. and to demonstrate the base line shifts observed in the

experiment. The calibration is performed by Rabi spectroscopy including the fast z pulsing scheme as adopted in successive quantum simulation experiments. The applied pulse sequence and measured Rabi oscillations are depicted in Fig. S3. The length of the applied excitation pulse is given on the horizontal axis in Fig. S3(b). Fundamental qubit states (black lines) can be mapped to dispersive shifts of the readout resonator with the bosonic mode in its groundstate and off-resonant.

Qubit basis shift

The qubit state is expected to assume an incoherent steady state on the equator of the Bloch sphere for long simulation times Δt due to the finite coherence in our circuit. However, we notice a shift in the steady state qubit population dependent on the initially prepared qubit state. This is apparent in Fig. S3(c), showing measurements for the qubit prepared in $|e\rangle$ (blue) and $|g\rangle$ (green) and in Fig. 3(f)-(i) in the main text. We attribute this effect to a change in the effective qubit basis, which is not captured by the master equation simulations performed. We additionally conjecture that the basis shifts are caused by an effective tilt of the qubit Bloch sphere as an artifact of the frequency tuning in experiment prior to applying the Rabi drives. We isolate the effect as an initialization issue since the basis shift cancels out in good approximation when averaging the mutually antiparallel simulation sequences in Fig. 3(f)-(i).

CLASSICAL MASTER EQUATION SIMULATION

Numerical simulations are based on a master equation solver provided by the QuTiP package [S6, S7] for python. The time evolution of a given initial state or density matrix is calculated by solving the von Neumann equation associated with the given system Hamiltonian in the absence of dissipation. For including losses to an imperfect environment of the system Hamiltonian, the time evolution of the density matrix is calculated via the Lindblad master equation.

Classical simulations in the main text include a finite lifetime of the qubit of about $5\text{ }\mu\text{s}$, a dephasing time of about $1\text{ }\mu\text{s}$ and a bosonic mode decay rate of $\kappa/2\pi \sim 0.5\text{ MHz}$. The Fock space of the bosonic mode is truncated at a photon number of 30, since higher excitation numbers were found to not play a significant role. The transmon qubit is treated as a three-level system with the experimentally found anharmonicity $\alpha/2\pi = -350\text{ MHz}$. We use a transversal qubit coupling operator

$$\sum_{ij} \hat{g}_{ij}^x \equiv \sum_{ij} \frac{g_{ij}}{g_{01}} |i\rangle \langle j|, \quad (\text{S17})$$

with the coupling matrix elements g_{ij} found by evaluating the Cooper pair number operator in the charge basis [S8, S9].

Since the qubit and the bosonic mode are on resonance during the experiment and both elements are spatially close by, the parasitic coupling of the applied drives to the bosonic mode is not zero. We account for the effected excess population of the bosonic mode by direct coupling in the simulation via a drive term of the form

$$(\hat{b}^\dagger + \hat{b})\eta_b \cos(\omega_1 t + \varphi_1), \quad (\text{S18})$$

with $\eta_b/\eta_1 \sim 3\%$.

Verifying the simulation scheme

Since a rotating frame is not an inertial system, the laws of physics may be drastically altered when describing a physical system in a rotating frame. In the framework of analog quantum simulation, this offers a rich toolbox which allows to access intriguing effective parameter regimes that are hard or impossible to access in the laboratory frame. Likewise one has to guarantee that the dynamics of the system is fully recovered in the rotating frame especially since some system parameters such as dissipation for instance are not transformed and remain valid in the laboratory frame. While the qubit dynamics is well reproduced as demonstrated in Fig 3 in the main text, it is not a priori clear that the bosonic mode population evolution is likewise well reflected in the simulation. To verify the simulation scheme we compare the bosonic mode population in the driven laboratory frame, and the expected evolution of the ideal

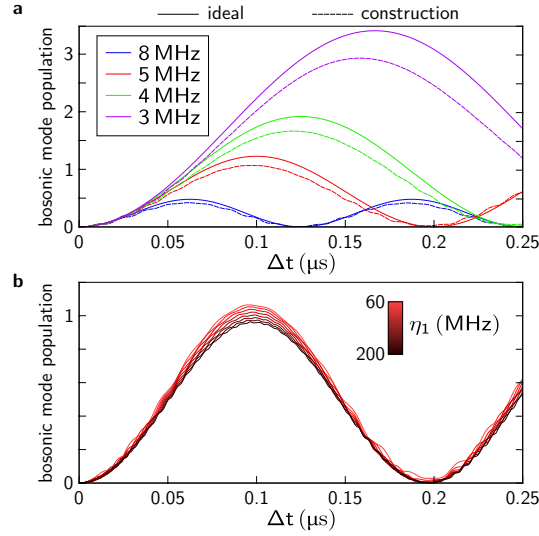


FIG. S4. (a) Time evolution of the bosonic mode population for a simulation sequence with $\eta_2 = 0$. We compare its population in the ideal quantum Rabi Hamiltonian (solid line) with the population of the bosonic mode in the laboratory frame with the drive applied (dashed line). Despite the fact that an infinite energy reservoir is supplied by the drive, the population follows the expected one rather well. This remains also true for varying the drive amplitude η_1 . Different colors correspond to a varying ω_{eff} . (b) Bosonic mode population for $\omega_{\text{eff}}/2\pi = 5$ MHz and a varying drive amplitude η_1 . The evolution and maximum population is confirmed to be independent of η_1 in first order. Master equation simulations here are performed without taking into account dissipation and neglect parasitic driving of the bosonic mode.

quantum Rabi model via classical master equation simulations. Here, we neglect dissipation and parasitic driving of the bosonic mode. Figure S4(a) demonstrates good agreement when comparing the time evolutions of the ideal (solid line) and the constructed (dashed line) Hamiltonians. The violation of excitation number conservation in the quantum Rabi model manifests in excitation numbers of the bosonic mode of larger than one for small ω_{eff} . We find that the maximum photon excitation in the bosonic mode roughly equals one for choosing simulation conditions where $\omega_{\text{eff}} \approx g = 2\pi \times 5$ MHz.

For $\omega_{\text{eff}}/2\pi = 5$ MHz we show that the population in the bosonic mode is independent of the applied drive amplitude η_1 that does not appear in the constructed Hamiltonian, Eq. (S12). Simulations for various η_1 are depicted in Fig. S4(b).

Qubit population retrieval from measured dispersive shifts of the readout resonator

In measuring the dispersive shift of the readout resonator during the quantum simulation experiment, we observe a bulged and shifted equatorial baseline following the expected population evolution of the bosonic mode as obtained from the master equation simulation. We attribute this to a cross-Kerr coupling λ between the bosonic mode and the readout resonator. By inheriting nonlinearity from the qubit it gives rise to a dispersive shift on the readout resonator dependent on the photon number in the bosonic mode. The complete Hamiltonian including the readout resonator of resonance frequency ω_r with creation (annihilation) operator \hat{a}^\dagger (\hat{a}) and with the RWA applied takes the form

$$\begin{aligned} \hat{H}/\hbar = & \frac{\epsilon}{2}\hat{\sigma}_z + \omega\hat{b}^\dagger\hat{b} + \omega_r\hat{a}_r^\dagger\hat{a}_r + g\left(\hat{\sigma}_-\hat{b}^\dagger + \hat{\sigma}_+\hat{b}\right) + g_r\left(\hat{\sigma}_-\hat{a}_r^\dagger + \hat{\sigma}_+\hat{a}_r\right) \\ & + \lambda\left(\hat{a}_r\hat{b}^\dagger + \hat{a}_r^\dagger\hat{b}\right) + \hat{\sigma}_x\eta_1\cos(\omega_1t + \varphi_1) + \hat{\sigma}_x\eta_2\cos(\omega_2t + \varphi_2). \end{aligned} \quad (\text{S19})$$

$g_r/2\pi \sim 55$ MHz denotes the coupling strength between qubit and readout resonator. The conjecture is verified by comparing simulations with the cross Kerr coupling λ switched on and off, respectively, see Fig. S5(a). As clearly visible in Fig. S5(b), the difference of both simulations (gray) follows the simulated evolution of the bosonic mode population (red). In addition, we isolate the dispersive shift $\propto \lambda^2$ induced by the cross-Kerr coupling between the bosonic mode and the readout resonator by adding up measured data for the qubit prepared either in $|g\rangle$ or $|e\rangle$. Comparison with measured data suggests $\lambda \sim$ MHz.

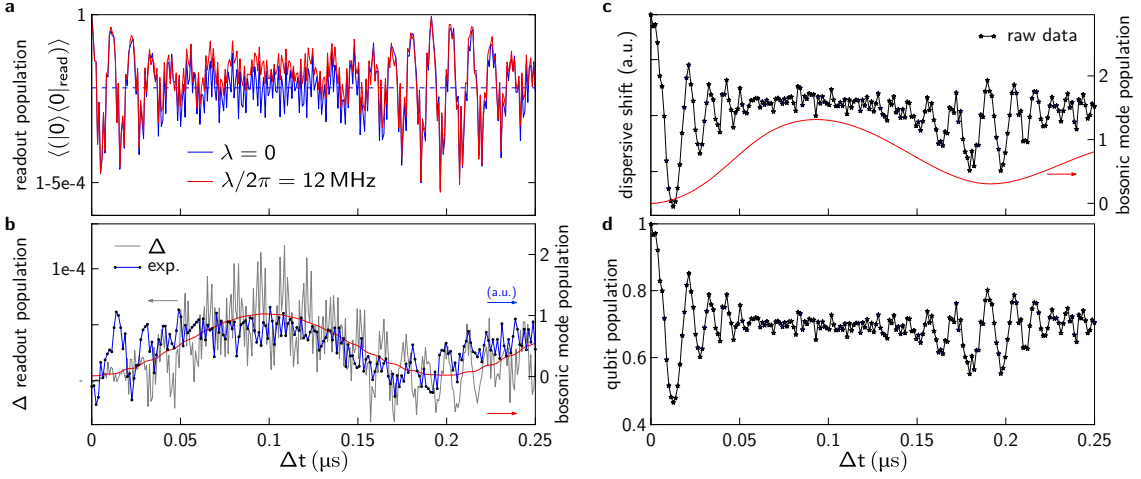


FIG. S5. Verification of cross-Kerr coupling between the bosonic mode and the readout resonator. (a) Expectation value of the vacuum projection $|0\rangle\langle 0|$ of the readout resonator state for vanishing cross-Kerr $\lambda = 0$ (blue) and for a cross-Kerr of $\lambda/2\pi = 12$ MHz (red), chosen for better visibility. The blue dashed line denotes the mean value of the $\lambda = 0$ simulation as a guide to the eye. (b) The difference between both simulations (gray) follows the simulated time evolution of the bosonic mode population (red), as obtained from the same simulation, and the dispersive shift extracted from experiment (blue). (c) Dispersive shift of the readout resonator including both the shifts induced by qubit and bosonic mode. The red line depicts the classically simulated population of the bosonic mode. (d) Pure qubit signal in the afore calibrated basis after extracting the shift of the bosonic mode.

QUANTUM REVIVALS FOR INITIAL QUBIT STATE $|g\rangle, |e\rangle$

We demonstrate that the position of the quantum revival corresponds to $2\pi/\omega_{\text{eff}}$ in quantum simulations with initial state prepared in $|0\rangle \otimes |g\rangle$, where both the qubit and the bosonic mode are in its groundstate. Classical simulations are done for $\kappa/2\pi \sim 0.5$ MHz and $T_1 = 5 \mu\text{s}$, $T_2 = 0.5 \mu\text{s}$.

We find a better agreement of experimental data with classical simulations for a slightly increased geometric coupling $g/2\pi \sim 5.5$ MHz as compared to the extracted value from vacuum Rabi oscillations of $g/2\pi = 4.3$ MHz. This might be an effect of higher levels of the transmon that is not captured in the vacuum Rabi experiment where the total excitation number is preserved and does not exceed one. With this effective geometric coupling we approach an ultra-strong coupling regime with $g_{\text{eff}}/\omega_{\text{eff}} \sim 0.7$ for the experiment depicted in Fig. S6(d).

VERIFICATION THE PARAMETER CONSTRAINT FOR $\eta_2 \neq 0$

We verify the simulation data for the full quantum Rabi model presented in the main text by comparison to measured data with intentionally departing from the required parameter constraints. While an increase in revival amplitude and an increased amplitude of the fast oscillations for larger Δt is visible by comparing Fig. S7(a), (b) presented in the main text, these signatures vanish for violating the parameter conditions

$$\begin{aligned}\varphi_1 &= \varphi_2 \\ \eta_1 &= \omega_1 - \omega_2\end{aligned}\tag{S20}$$

required by the simulation scheme. We chose $\varphi_1 \sim \varphi_2 + \pi$ but $\eta_1 = \omega_1 - \omega_2$ in Fig. S7(c) and $\omega_2 = \omega_1 - \eta_1 - 2\pi \times 10$ MHz while $\varphi_1 = \varphi_2$ in Fig. S7(d) in order to demonstrate that the desired experimental features vanish.

SPECTROSCOPY OF THE AVOIDED CROSSING BETWEEN QUBIT AND BOSONIC MODE

The coupling between qubit and bosonic mode is pre-characterized in a spectroscopy measurement using a vector network analyzer. The dispersive readout resonator shift is measured with a continuous microwave tone while an additional drive tone is applied through the same transmission line to excite the qubit transition. The fit of the observed avoided crossing yields a minimum line separation of $2g/2\pi = 7.8$ MHz.

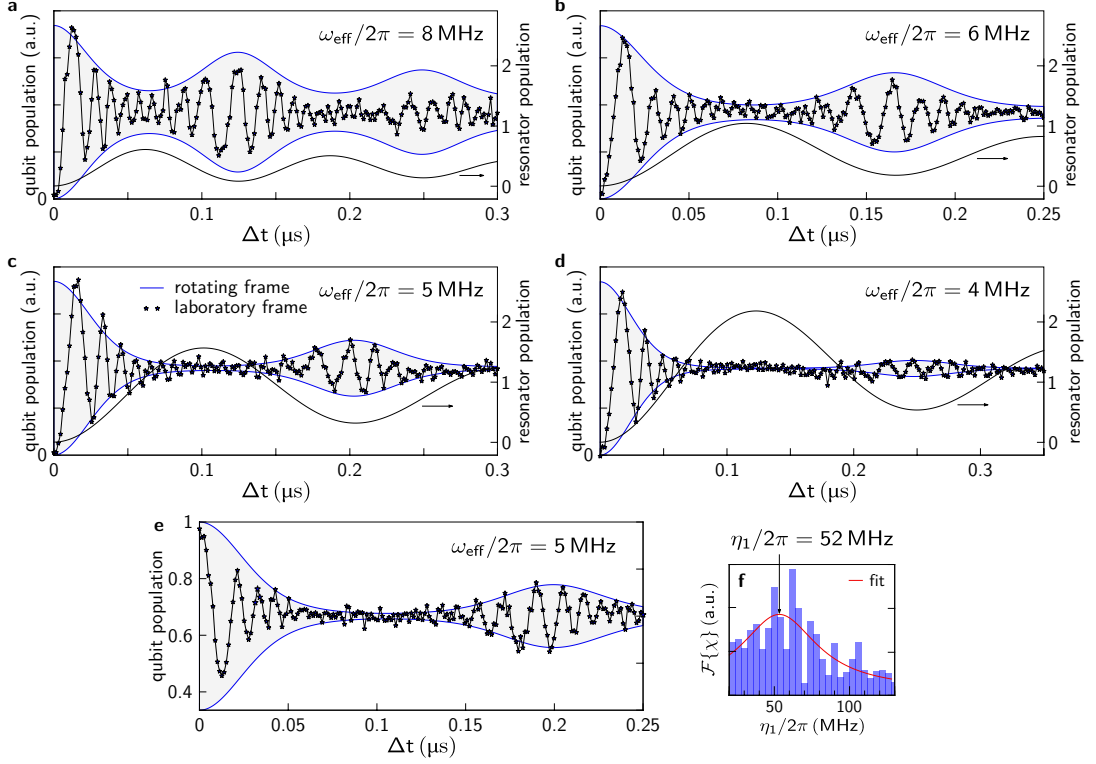


FIG. S6. Quantum collapse and revival signatures for various effective energies ω_{eff} of the bosonic mode. (a)-(d) The qubit is prepared in its groundstate and the bosonic mode is initially in the vacuum state, $|0\rangle \otimes |g\rangle$. The first revival appears at $2\pi/\omega_{\text{eff}}$, respectively. The blue line corresponds to the classical simulation of the ideal Hamiltonian in the rotating frame, plotted in the two-level qubit basis. The shift in qubit basis is subtracted in order to compare quantum simulation and classical master equation simulation. The black line shows the classically simulated population of the bosonic mode, which increases with decreasing ω_{eff} . (e) Quantum simulation with the qubit prepared in $|e\rangle$. From Fourier transformation (f) we obtain $\eta_1/2\pi = 52$ MHz.

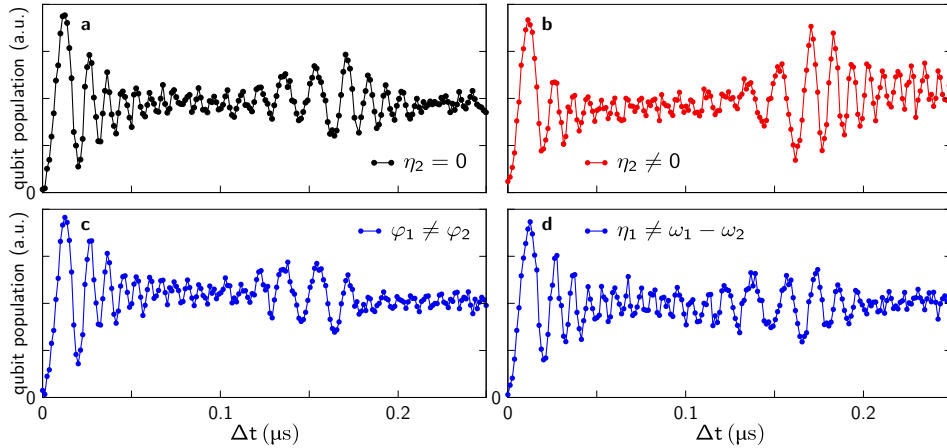


FIG. S7. Verification of the parameter constraint for $\eta_2 \neq 0$. Measurements for $\eta_2 = 0$ (a) and the proper parameter choice when $\eta_2 \neq 0$ (b) are compared to measurements with parameters violating the phase matching condition, $\varphi_1 \neq \varphi_2$ (c) and $\eta_1 \neq \omega_1 - \omega_2$. When the required constraint are not satisfied, the revival amplitude is decreased and the oscillation amplitude remains small for all Δt . The dispersive shift of the readout resonator induced by the bosonic mode is subtracted based on classically simulated data.

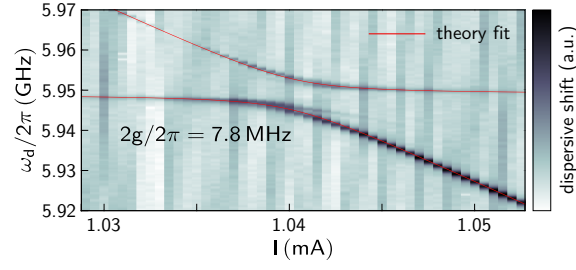


FIG. S8. Avoided crossing between qubit and bosonic mode in spectroscopy. The qubit transition frequency is tuned by a dc current applied to the flux coil. The dispersive shift of the readout resonator is proportional to the excitation number of the qubit and is depicted in colors.

* jochen.braumueller@kit.edu.

- ^{S1} D. Ballester, G. Romero, J. J. García-Ripoll, F. Deppe, and E. Solano, Phys. Rev. X **2**, 021007 (2012).
- ^{S2} A. Leggett, S. Chakravarty, A. Dorsey, M. Fisher, A. Garg, and W. Zwerger, Rev. Mod. Phys. **59**, 1 (1987).
- ^{S3} E. Jaynes and F. Cummings, Proc. IEEE **51**, 89 (1963).
- ^{S4} J. Braumüller, M. Sandberg, M. R. Vissers, A. Schneider, S. Schlör, L. Grünhaupt, H. Rotzinger, M. Marthaler, A. Lukashenko, A. Dieter, A. V. Ustinov, M. Weides, and D. P. Pappas, Appl. Phys. Lett. **108**, 032601 (2016).
- ^{S5} A. Lukashenko and A. V. Ustinov, Rev. Sci. Instrum. **79**, 014701 (2008).
- ^{S6} J. Johansson, P. Nation, and F. Nori, Comp. Phys. Comm. **183**, 1760 (2012).
- ^{S7} J. Johansson, P. Nation, and F. Nori, Comp. Phys. Comm. **184**, 1234 (2013).
- ^{S8} J. Koch, T. M. Yu, J. Gambetta, A. A. Houck, D. I. Schuster, J. Majer, A. Blais, M. H. Devoret, S. M. Girvin, and R. J. Schoelkopf, Phys. Rev. A **76**, 042319 (2007).
- ^{S9} J. Braumüller, J. Cramer, S. Schlör, H. Rotzinger, L. Radtke, A. Lukashenko, P. Yang, S. T. Skacel, S. Probst, M. Marthaler, L. Guo, A. V. Ustinov, and M. Weides, Phys. Rev. B **91**, 054523 (2015).